Calibration monitoring of the visible and near-infrared channels of the Along-Track Scanning Radiometer-2 by use of stable terrestrial sites

Dave L. Smith, Chris T. Mutlow, and C. R. Nagaraja Rao

The Along-Track Scanning Radiometer-2 (ATSR-2) is equipped with visible and near-infrared channels at 1.6, 0.87, 0.66, and 0.56 μm. An in-flight visible calibration (VISCAL) system used to convert the raw signal to top-of-the-atmosphere reflectances is described. To monitor the long-term stability of the VISCAL, a number of large-area stable terrestrial sites have been employed. We describe the methods used to determine the long-term drifts in the ATSR-2 onboard calibration device and evaluate the suitability of the sites for calibration monitoring. © 2002 Optical Society of America

OCIS codes: 120.0280, 120.5630.

1. Introduction

The Along-Track Scanning Radiometer (ATSR-2) instrument on the European Space Agency's (ESAs) European Remote Sensing Satellite-2 (ERS-2) Satellite is designed to measure sea surface temperatures to better than 0.3 K accuracy, monitor global vegetation cover, and provide observations from which aerosol and cloud properties can be retrieved. Infrared channels at 3.7, 10.8, and 12 μm measure thermal emission from the Earth's surface and overlying atmosphere; and the visible and near-infrared (VNIR) channels at 0.56, 0.66, 0.87, and 1.6 μm measure reflected solar radiation. A conical scanning geometry allows the collection of images of the same scene through two atmospheric paths: a nadir view and a forward along-track view at 55° zenith angle. When we use the results of atmospheric modeling, data from both views in the VNIR channels can be combined to retrieve the aerosol optical thickness, cloud optical properties, and improved surface reflectance.[1]

The usefulness of geophysical products derived from measurements of the diffusely reflected radiation at the top of the atmosphere (TOA) in the ATSR-2 VNIR channels in climate and weather studies, and in the detection of long-term trends in climate, is determined by the accuracy of the satellite radiation measurements and the in-orbit stability of the radiometer. It is thus necessary to monitor the in-orbit performance of the instrument in view of the fact that the performance of satellite radiometers in the VNIR degrades after launch because of the deleterious effects of exposure to the harsh space environment and outgassing.[2] For example, annual degradation rates of approximately 6% have been observed in the VNIR channels of the advanced very high resolution radiometer (AVHRR) flown on the National Oceanic and Atmospheric Administration's (NOAA's) polar orbiters.[3,4] In addition to these long-term effects, the instruments may also be subject to short-term fluctuations in the signal that are due to instability of electrical power supplies or, as in the case of ATSR-2, the gradual buildup of condensation on cooled optical surfaces.[5] It is therefore important to devise effective vicarious means of monitoring the performance of satellite radiometers in orbit, even when onboard calibration capability exists as in the case of the ATSR-2. Accordingly, we describe here the monitoring of the ATSR-2 in-orbit calibration using nine radiometrically stable calibration sites around the globe, using techniques similar to those employed by previous researchers, to characterize the in-orbit performance of the VNIR channels of the AVHRR.[3,6,7]

D. L. Smith (d.l.smith@rl.ac.uk) and C. T. Mutlow are with Rutherford Appleton Laboratory, Council for the Central Laboratory of the Research Councils, Didcot, Oxfordshire OX11 0QX, United Kingdom. C. R. Nagaraja Rao (deceased) was with the National Oceanic and Atmospheric Administration, National Environmental Satellite, Data, and Information Service, Office of Research and Applications, Washington, D.C. 20233.

Received 29 January 2001; revised manuscript received 28 September 2001.

0003-6935/02/030515-09$15.00/0

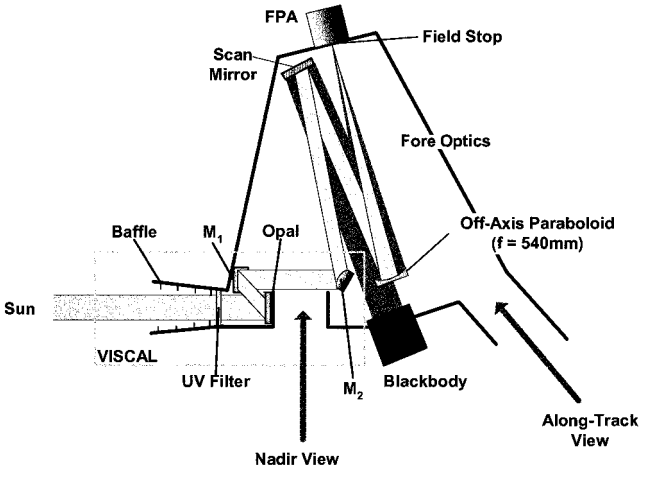

Fig. 1. Schematic diagram of ATSR-2 showing the VISCAL system. FPA, focal-plane assembly.

2. Determination of Earth Scene Reflectance

A. General

The ATSR-2, unlike the AVHRR, has an onboard calibration device for the VNIR channels. The multisite postlaunch calibration of the instrument thus characterizes the performance of the entire system, the radiometer, and the onboard visible calibrator (VISCAL). We first briefly describe the VISCAL system before giving details of the determination of Earth scene reflectance. The Earth scene reflectance data are central to the monitoring of ATSR-2 calibration in orbit.

B. Visible Calibrator

Two onboard reference targets are used in the calibration of the VNIR channels (Fig. 1). The zero-radiance signal is obtained from data collected over one of the onboard blackbodies used for the thermal channel calibration, and the upper radiance measurement in the calibration is provided by the VISCAL unit.[8] The VISCAL unit consists of a diffuser plate (matt Russian Opal type MS20) that is illuminated by the Sun at normal incidence by a baffled tube. Two mirrors (M_1 and M_2 in Fig. 1) reflect light scattered at 45° into the main instrument fore optics. The baffle tube is used to restrict stray light from the atmosphere and satellite, but limits the calibration period to 30 s/orbit. A blocking filter reduces degradation of the diffuser plate from exposure to UV radiation and also the fluorescence signal from the UV. A photodiode monitor mounted through the center of M_2 is used to detect any changes in the surfaces of the opal and mirror M_1. Both calibration targets (the VISCAL and the blackbody) are arranged so that they are viewed every rotation of the scan mirror. The system provides a signal L_{scene} corresponding to a reflectance R_{VISCAL} relative to 100% reflectance from a Lambertian surface at normal solar incidence. Thus R_{VISCAL} is given by

$$R_{\text{VISCAL}} = [\alpha\pi(C_{\text{VISCAL}} - C_{\text{dark}})/\text{gain}]/(I_{0,\lambda}d\lambda), \quad (1)$$

Table 1. ATSR-2 Signal Channel Bandwidths and VISCAL Reflectance Factors

Channel (μm)	$d\lambda$ (μm)	R_{VISCAL}
0.56	0.019	0.119 ± 0.002
0.66	0.021	0.119 ± 0.002
0.87	0.021	0.110 ± 0.002
1.6	0.067	0.141 ± 0.003

where α is the radiometric response of the instrument determined in the prelaunch environment; gain is the commanded gain; and C_{VISCAL} and C_{dark} are, respectively, the radiometer signals in counts when the instrument is looking at VISCAL and the blackbody target; $I_{0,\lambda}$ is the extraterrestrial solar irradiance (in $\text{Wcm}^{-2}\ \text{sr}^{-1}\ \mu\text{m}^{-1}$) at the central wavelength of the given channel; and $d\lambda$ is the bandwidth. The approximation for the solar irradiance $I_{0,\lambda}d\lambda$ is used because the bandwidths of the ATSR-2 visible channels are relatively narrow and there are no significant absorption features present. The ATSR-2 channel bandwidths are given in Table 1.

C. Earth Scene Reflectance

From the VNIR data, the bidirectional reflectance function (BRDF) of an Earth scene R_{scene} at wavelength λ can be determined with

$$R_{\text{scene}} = (\pi L_{\text{scene}})/(\mu_0 I_{0,\lambda}d\lambda), \quad (2)$$

where L_{scene} is the measured scene radiance and μ_0 is the cosine of the solar zenith angle θ_0. The scene radiance (in units of $\text{Wcm}^{-2}\ \text{sr}^{-1}$) is given by

$$L_{\text{scene}} = \alpha(C_{\text{scene}} - C_{\text{dark}})/\text{gain}, \quad (3)$$

where C_{scene} is the instrument response in counts when it is looking at the Earth scene. This is similar to the standard method used for other satellite radiometers such as the AVHRR and the Landsat Thematic Mapper. The radiometric responses of the 0.56-, 0.66-, and 0.87-μm signal channels (i.e., the combined response of the instrument fore optics, filters, detector, and preamplifier system) were measured prior to launch to an accuracy of ~5%. The 1.6-μm signal channel response was not calibrated prior to launch because there was originally no requirement to do so. However, the 1.6-μm channel is calibrated through the VISCAL system.

Combining Eqs. (1), (2), and (3), for the Earth scene reflectance, we obtain

$$R_{\text{scene}} = R_{\text{VISCAL}}[(C_{\text{scene}} - C_{\text{dark}})/(C_{\text{VISCAL}} - C_{\text{dark}})]\mu_0. \quad (4)$$

The VISCAL reflectance factor R_{VISCAL} determined from the properties and geometry of the optical components is given in Table 1. It should be noted that the assumption of long-term temporal stability and spatial homogeneity of R_{scene} is central to the postlaunch calibration trend monitoring of ATSR-2 by use of multiple terrestrial sites.

Table 2. Calibration Sites used in the Study

Site	Longitude Range	Latitude Range
Algeria (East)	7°10′ E–8°10′ E	29°49′ N–30°49′ N
Algeria (West)	0°42′ E–1°42′ E	30°30′ N–31°18′ N
Arabia	46°16′ E–47°16′ E	18°23′ N–19°23′ N
Dunhuang	94°01′ E–94°30′ E	40°02′ N–40°17′ N
Libya 1	12°31′ E–13°31′ E	23°55′ N–24°55′ N
Libya 2	10°49′ E–11°49′ E	25°59′ N–26°59′ N
Sudan	28° W–29° W	21° N–23° N
Sechura	80°42′ W–80°18′ W	6°12′ S–5°48′ S
Sonora	114°18′ W–113°54′ W	31°54′ N–32°06′ N
Greenland	35° W–45° E	70° N–77.5° N

Table 3. ATSR-2 Pixel Maps

Format	Channels	Nadir (km)	Along Track (km)
H-rate	All	555	555
L-rate map 14	IR channels	555	555
	0.87 and 0.66 μm	555	555 interlaced
	0.56 μm	300	1
L-rate map 13	IR channels	555	555
	Visible channels	180	180

3. Description of the Calibration Sites

A. General

The choice of the sites was guided by the research already reported in the literature on the postlaunch calibration of the AVHRR and the Geostationary Operational Environmental Satellite (GOES) imager.[3,4,6,9] As mentioned above, radiometric stability of the calibration sites implies long-term stability of the TOA albedo (and of seasonal variations, if any) or reflectance over large spatially uniform areas. It should be noted that ATSR-2 measures a BRDF that varies with surface anisotropy and other angular effects and must be accounted for when we are determining long-term calibration trends. This is addressed in Section 4.

Another desirable feature is to have high surface reflectance to maximize the signal-to-noise ratio and minimize atmospheric effects on the radiation measured by the satellite. In addition, low incidence of clouds would enhance the usefulness of the site. After a careful survey of past and current usage and of available metadata[10] about the sites, nine sites listed in Table 2 were chosen for the present study. These include desert sites in Algeria, Arabia, China, Libya, Mexico, and Peru, and the large ice sheets of Greenland. The choice of sites gives a wide range of measurements as indicated in Fig. 4 for the 0.87-μm channel. Comparison of the calibration results should identify those sites most suited for long-term monitoring.

The combination of high surface reflectance, long-term stability, and spatial homogeneity render these sites ideal for calibration trend monitoring and comparison of the in-orbit performance of similar instruments. A limitation, however, is that ground-based measurements of surface reflection and other surface index properties and of meteorological variables are not generally available for a large number of sites chosen.

B. Image Processing

ATSR-2 images for each of the sites were generated from the start of the mission in May 1995 to September 2000. All images contained nadir and along-track 0.56, 0.66-, 0.87-, and 1.6-μm pixel counts and 11- and 12-μm brightness temperatures. We calibrated the visible channel images using Eq. (4) with the coefficients derived from the onboard calibration data.

For most of the sites in this study, data for all ATSR-2 channels were transmitted at 12-bit digitization for the full swath width of 555 km, referred to as H-rate format. However, it is not always possible to obtain H-rate data because of a limit in the ERS-2 telemetry bandwidth. When the Wind Scatterometer instrument on the ERS-2 payload is used (usually over oceans), ATSR-2 is forced to transmit a reduced L-rate format, at the expense of the visible channels. This affects all scenes within 200 km of a coastline such as the Sechura, Sonoran, and Arabian deserts Greenland. The strongest impact was on the Sechura Desert site where no H-rate data at all were recorded. The content of transmitted data in L-rate depends on the compression modes used and more importantly the pixel map being used. A summary of the operational data formats is given in Table 3. In L-rate format the 11- and 12-μm data are transmitted as a 12-bit 11-μm channel and an 8-bit 11–12-μm difference. The 3.7- and 1.6-μm channels are transmitted as 10-bit 3.7-μm or 10-bit 1.6-μm channels if the signal exceeds a prespecified count limit. The short-wavelength channels are transmitted as 5-bit exponent and 3-bit mantissa.

The TOA radiance or reflectance is affected by surface reflection properties and surface conditions, viewing and illumination geometry, cloud cover, and absorption and scattering by the gaseous and aerosol components. In particular, the presence of clouds, wet sand, dust, and vegetation generally increases the spread of reflectances and may bias the measurements, resulting in a less reliable calibration. The effects are slightly different for deserts and ice and are therefore described separately.

1. *Desert Sites*

Surface state. The North African and Saudi Arabian desert sites consist mainly of sand, gravel, and rocky outcrops and are arid with little or no vegetation. The sites are uniform over a large area with variations in reflectances less than 2%. The Dunhuang site on the northwest edge of the Gobi Desert in China has been well characterized and is uniform over a 30×40 km^2 area.[11] The area is an alluvial plain comprising a mixture of gravel, sand, and dust; and the surface reflectances are low compared with the North African and Saudi Arabian sites because of

the surface composition. The site is approximately 1.2 km above sea level, with an arid climate and clear atmosphere. The Sonoran Desert in Mexico is a semiarid region with limited vegetation cover, and there are some seasonal variations in the surface properties. The Sechura Desert is located on the north coast of Peru between the Andes and the Pacific Ocean. The selected area is a shallow riverbed and is at an altitude between 50 and 300 m above sea level. Use of this site has been compromised because, during the 1997 El Niño event, severe flooding occurred and the area became a large lake. Therefore only data up to November 1997 could be used in this study.

Clouds and dust. The basic assumption made about the desert sites is long-term stability. However, there is often some level of cloud cover and occasional precipitation. Clouds have a higher reflectance than the underlying scene, whereas the reflectance of wet sand is lower. Moreover, dust storms occur frequently and generally lower the measured TOA albedo when the surface reflectance is high. All three phenomena produce a lower brightness temperature than for clear desert.[6] However, because of the spatial uniformity of the sites chosen, clouds, wet sand, and dust will increase the noise in TOA radiances measured over an area.

Each ATSR-2 image was split into 4 km $\times$ 4 km regions and the ranges (maximum and minimum) of 1.6-μm reflectance and 11- and 12-μm brightness temperatures of each region were calculated ($\Delta R_{1.6\ \mu m}$, $\Delta T_{11\ \mu m}$, and $\Delta T_{12\ \mu m}$). Data from the short-wavelength channels were not used for cloud detection because the compression modes of ATSR-2 meant that some channels were not always present in an image. Image regions were declared as cloudy pixels if $\Delta R_{1.6\ \mu m}/R_{1.6\ \mu m} > 0.1$, $\Delta T_{11\ \mu m}/T_{11\ \mu m} > 0.01$, and $\Delta T_{12\ \mu m}/T_{12\ \mu m} > 0.01$. The spatial test worked well for cumulus, cirrus, localized dust storms, and wet sand, but was less effective at detecting large areas of stratus. Pixels that passed the spatial coherence checks were tested for low brightness temperatures. During the daytime, deserts are generally hot with brightness temperatures >290 K, whereas clouds are cooler. The temperature at the peak of the temperature histogram for the image T_{peak} is compared with the maximum brightness temperature T_{max}. If $T_{max} - T_{peak} < 25°$, then pixels with brightness temperatures outside the main peak are rejected. If the $T_{max} - T_{peak} > 25°$, it is likely that there is more cloud than desert and the whole image is declared cloudy.

Ozone absorption. For the desert sites, there are seasonal variations in ozone concentrations that have a small effect on the TOA reflectances at 0.56 μm ($\sim$1%) because of absorption in the Chappuis bands.[12] However, it was not necessary to make any correction for ozone absorption because the effect on the trend detection was negligible.

2. Greenland Ice

Alternatives to use of desert scenes for trend analysis are the icecaps of Greenland and Antarctica.[9] The ice sheets cover a large area and can be assumed to be temporally stable. The area used for this study was the region of the Greenland icecap bounded by 70° N–77.5° N, 35° W–45° W, where the ice sheet is >2 km above sea level. In this region the surface slope is low and so no corrections to the view and solar geometry were necessary.

Surface state. As with the desert sites, it is assumed that the properties of the ice sheet are stable over many years. At altitudes >2 km, the ice sheet consists of compacted snow and does not melt because of the low surface temperatures. Multiple scattering calculations were used to model the bidirectional reflectance of deep snow and predict the effects of solar zenith angle and grain size.[13] The research in Ref. 13 predicts that, at wavelengths <0.7 μm, there is little absorption and so the total albedo of snow is high and relatively independent of solar zenith angle. At longer wavelengths, the absorption coefficient increases and hence the albedo will be lower and more dependent on solar zenith angle, becoming higher at low Sun. The scattering phase function of snow particles is asymmetric, hence the BRDF varies significantly with solar zenith angle. At high Sun, the BRDF is close to Lambertian, whereas at low Sun it has a strong forward peak. Snow grains vary in size between 50 and 1000 μm depending on their age. The effect of grain size is most significant in the near infrared, where the albedo can vary by a factor of 2 over the range of sizes. At the visible wavelengths, the effect is less significant with typical variations of only a few percent.

Clouds. Identification of clouds over ice is difficult because their reflective and thermal properties are similar at the ATSR-2 wavelengths. The presence of clouds in an ice scene will generally increase the spread of the TOA radiance. As with Loeb,[9] the basic approach is to consider the spatial uniformity of the scene to determine the cloud cover; although the procedure used here differs somewhat from that method, the underlying principle remains the same.

Images were divided into 4 km $\times$ 4 km regions in the same way as for the desert scenes, and the ranges of 0.87-μm reflectances $\Delta R_{0.87\ \mu m}$ and 12-μm brightness temperatures $\Delta T_{12\ \mu m}$ were determined for each separate region. The thresholds chosen to define cloudy pixels were $\Delta R_{0.87\ \mu m} > 0.5\%$ and $\Delta T_{12\ \mu m} > 0.5$ K. In a few cases, this test was insufficient to identify all clouds, particularly when they covered a large area. We overcame this by utilizing the distribution of the 1.6-μm channel reflectance to identify the remaining cloudy pixels. For snow the reflectance at 1.6 μm is low, <10%, depending on composition.[13] Ice (or supercooled water) clouds overlying the snow surface generally increase the scene reflectance because of the relatively small crystal size and correspondingly high scattering efficiency. It is worth noting that typical stratiform clouds found in

these regions have smaller ice crystals than more convectively active clouds of lower latitudes (some deep convective clouds have reflectances <10%). After rejecting pixels that failed the spatial uniformity criteria, we found a few pixels with higher reflectances (>20%) corresponding to the more uniform clouds.

After identifying the clouds, we calculated the average, maximum, minimum, and standard deviations for each channel reflectance for 16 km × 16 km regions. A flag was set to indicate if the area was cloud free. This process was repeated for all the Greenland images collected between May and August of each year.

Ozone. For high latitudes, ozone absorption at the 0.66- and 0.56-μm channels must be considered. The effect of ozone on the TOA signal is significant because of the range of illumination angles and the high seasonal variability of the ozone column. The corrected reflectance is given by

$$R' = R/\tau_{\text{ozone}}. \tag{5}$$

The transmission τ_{ozone} through the ozone column, assumed to be concentrated in a thin layer at the TOA, is given by

$$\tau_{\text{ozone}} = 1 - (\sec\theta + \sec\theta_0)\sigma\chi, \tag{6}$$

where σ is the absorption cross section in cm^2/molecule and χ is the ozone column in molecules cm^{-2}.[12] Contemporaneous Global Ozone Monitoring Experiment (GOME) ozone column retrievals were used to derive the corrections.

Viewing and illumination geometry. A significant limitation of the icecaps as a calibration site is the lower solar elevation. At large zenith angles the measured reflectance becomes increasingly sensitive to small variations in the satellite zenith angle, surface slope, and sastrugi.[14] The analysis is therefore restricted to values of $\theta_0 < 70°$, which therefore limits the period in which data can be used to a few months of each year.

Because of the latitude and the size of the area, the range of view and solar azimuth angles are larger than that for the desert sites. Restricting the data used in the calibration to nadir-only data, the measured reflectance becomes largely independent of relative azimuth.

4. Calibration Monitoring with Multiple Sites

Monitoring the calibration of the VNIR channels of the ATSR by use of terrestrial sites is attributed to the earlier research on the postlaunch calibration of the visible (channel 1, ≈0.58–0.68 μm) and near infrared (channel 2, ≈0.72–1.1 μm) of the AVHRR in which radiometrically stable desert sites were used[3,6,9] in the absence of onboard calibration devices. The southeastern Libyan Desert site, identified as the Sudan site in Table 2, was successfully used by Staylor[6] and by Rao and Chen[3] to assess the in-orbit degradation of, and determine the postlaunch calibration coefficients for, channels 1 and 2 of the AVHRRs on the NOAA-6, NOAA-7, NOAA-9, NOAA-11, and NOAA-14 spacecraft.

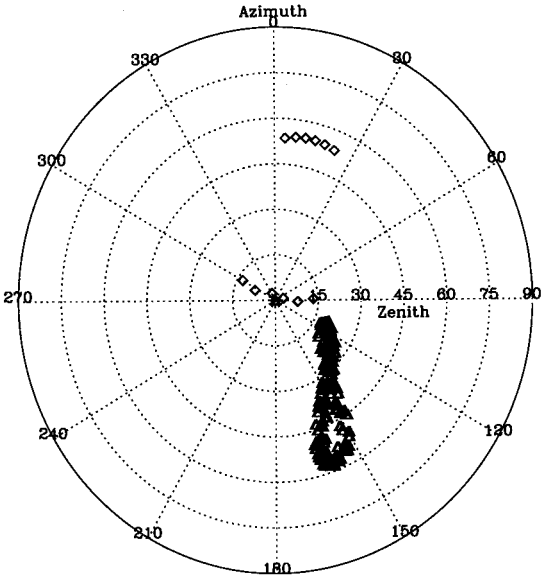

Fig. 2. Satellite (diamonds) and solar (triangles) geometry for the Sonoran Desert observations, typical of all the desert sites used in this study.

Once cloud-free images are selected, the measured reflectance will mainly be a function of the surface anisotropy $\hat{R}$ (θ, θ_0, φ, φ_0) and the calibration drift $D(t)$, where φ and φ_0 are, respectively, the satellite and solar azimuth angles and t is time. The drift and anisotropy functions are independent of each other because the surface is assumed to be radiometrically stable, so the measured scene reflectance can be expressed as

$$R_{\text{scene}} = \hat{R}(\theta, \theta_0, \varphi, \varphi_0)D(t). \tag{7}$$

To obtain the long-term drift it is necessary first to determine the anisotropy function. In Fig. 2 a typical example of the view and illumination geometry is shown for the Sonora site from 1995 to 2000. The site was observed at up to nine different azimuth angles in each of the instrument views during the 35-day repeat cycle. The variation in the range of view angles is limited because of the relatively narrow swaths of ATSR-2. ERS-2 is on a Sun-synchronous morning orbit, i.e., crossing the equator from north to south in the morning at 10:30 a.m., and hence the main variation in solar geometry is seasonal. These plots illustrate the stability of the ERS-2 orbit because the solar geometry does not drift over a long period. Because of these conditions, the scattering angle γ for each view angle, defined by

$$\begin{aligned} -\cos(180 - \gamma) = & \\ & \times \cos\theta \cos\theta_0 + \sin\theta \sin\theta_0 \\ & \times \cos(\varphi - \varphi_0), \end{aligned} \tag{8}$$

is a continuous and stable function.

Plotting the measured 0.87-μm reflectances

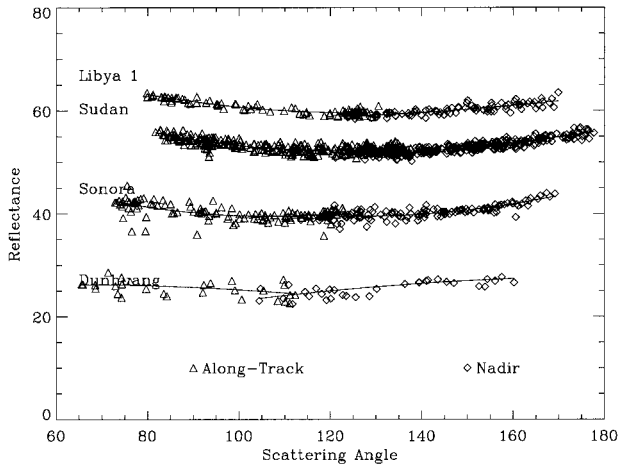

Fig. 3. Shown are the 0.87-μm reflectance versus scattering angle for Libya 1, Sudan, Sonoran, and Dunhuang deserts. Data for all view angles are included, and drift correction was applied.

against γ for the Libya 1, Sudan, Sonoran, and Dunhuang sites (Fig. 3), it can be seen that for most scene types there is an overlap between the nadir and along-track data at $110° < \gamma < 130°$. This could be interpreted as an indication of the seasonal stability because there is a six-month separation between the data for each view. Hence it is possible to treat the anisotropy as a simple function of γ, i.e.,

$$\hat{R} = a_0 + a_1\gamma + a_2\gamma^2. \tag{9}$$

The function was fitted to nadir and along-track data separately. The rms differences between the data and the model resulting from the least-squares fitting were typically ~1% for most sites with the exception of the Sechura site (Table 4). The higher differences for the Sechura data may be due to the poor number of cloud-free samples and some undetected cloud contamination in the data. The area is prone to mist because of the low altitude and the proximity to the cool waters of the Eastern Pacific.

The ozone-corrected, cloud-free reflectances of the Greenland icecaps for 1997 are shown in Fig. 4. Data for 2000 had not been analyzed at the time of this writing. As with the desert scenes, the measured reflectance could be expressed as a function of the scattering angle γ. However, because only nadir measurements were considered in this case, $-\cos(180 - \gamma) = \cos(\theta_0)$; hence the anisotropy function is expressed as

$$\hat{R} = a_0 + a_1 \cos\,\theta_0. \tag{10}$$

No higher-order terms were used for the ice data because they produced regression results that were too sensitive to outlying points and were therefore less repeatable. A linear function is adequate for this study because the purpose of the reflectance function is to approximate the variation with solar geometry to enable the long-term calibration drift to be estimated.

Table 4. Rms Differences of Least-Squares Fit of Polynomial through Reflectances as a Function of Scattering Angle

	Channel (μm)							
	1.6		0.87		0.66		0.56	
Site	Nadir	Along	Nadir	Along	Nadir	Along	Nadir	Along
Algeria (East)	0.9	0.6	1.1	0.9	0.8	0.8	1.0	1.0
Algeria (West)	0.9	0.8	1.1	1.2	0.9	1.1	0.7	0.9
Arabia	0.8	0.8	1.0	1.1	0.8	0.9	0.9	1.0
Dunhuang	1.6	1.8	1.3	1.4	0.6	1.2	0.4	1.0
Libya 1	0.7	0.6	1.2	1.1	1.0	1.1	1.0	1.1
Libya 2	1.2	1.4	0.9	1.6	0.9	0.9	1.1	1.1
Sudan	0.7	0.7	0.9	1.0	0.8	0.9	0.9	1.0
Sechura	2.7	—	2.1	—	1.8	—	2.0	—
Sonora	1.0	1.7	1.0	1.4	1.0	1.3	0.6	0.9

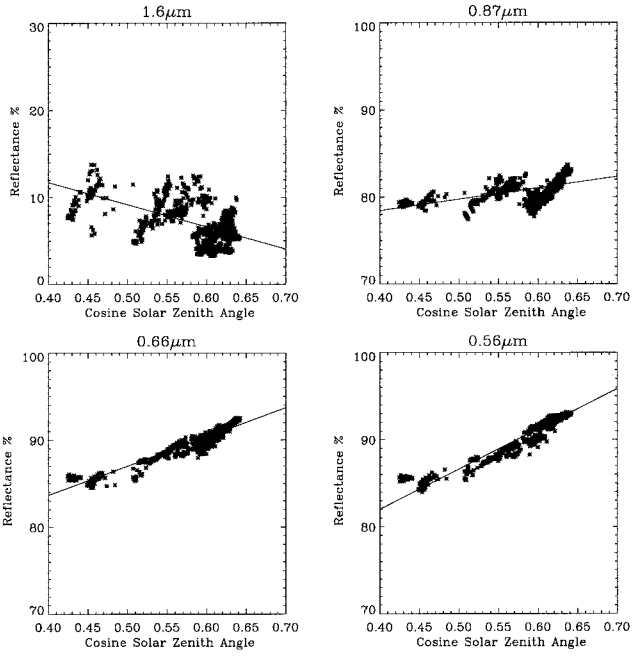

Fig. 4. ATSR-2 reflectance for Greenland for 1997.

5. Results

It should be noted that the ATSR-2 has the onboard calibration device, VISCAL, as opposed to the AVHRR channels 1 and 2 that have no onboard calibration devices. Thus, as mentioned above, the objective of the present study is to characterize the performance of the ATSR-2 and the VISCAL taken together as a system. The measured TOA reflectances are normalized to the anisotropy functions [i.e., $R/\hat{R} = D(t)$] for the various desert sites and the Greenland ice sheet and plotted as a time series to determine the trend, if any, in the calibration and in-orbit performance of the ATSR-2. The most noticeable feature is a gradual increase in measured reflectances for all channels as can be seen in the results from Algeria (West), a typical desert scene, and the Greenland ice sheet shown in Figs. 5 and 6, respectively. It can be seen that the rate of change decreases at the longer wavelengths. By fitting

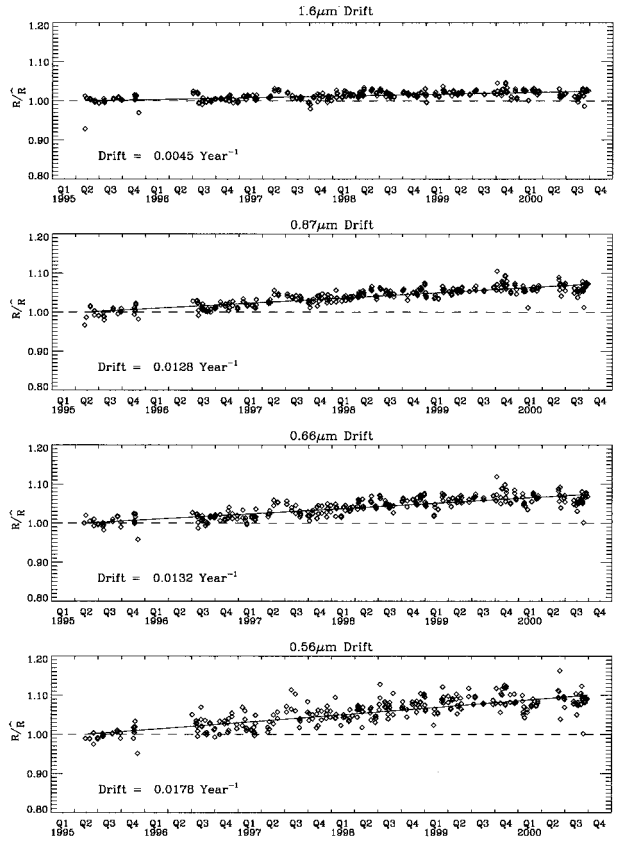

Fig. 5. Drift of normalized reflectances over the Algeria (West) site.

the function $D(t) = \exp(-kt/365)$ to the data, we can obtain the drift rates k, which are presented in Table 5 for all the sites in this study. For most sites, the results are consistent with the averages.

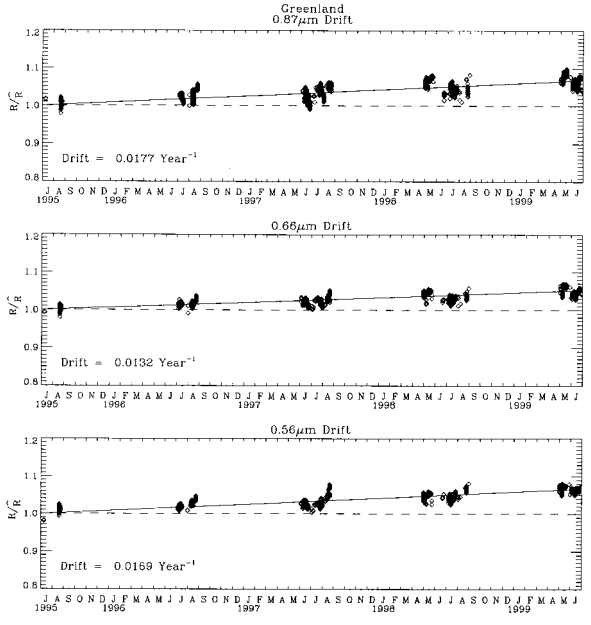

Fig. 6. Drift of normalized reflectances over Greenland.

Table 5. Percentage Calibration Drift Rate per Year

Site	Channel (μm) 1.6	0.87	0.66	0.56
Algeria (East)	0.2	1.0	1.1	1.7
Algeria (West)	0.4	1.3	1.3	1.8
Arabia	0.5	1.0	0.8	1.4
Dunhuang[a]	−0.5	0.0	−0.1	0.4
Libya 1	0.3	0.9	1.1	1.6
Libya 2	0.4	1.0	1.2	1.9
Sudan	0.1	0.9	0.9	1.4
Sechura[a]	−0.1	1.4	−1.0	0.6
Sonora[a]	0.8	1.6	1.6	1.6
Greenland	—	1.8	1.3	1.7
Average	0.3	1.1	1.1	1.6
Standard deviation	0.1	0.3	0.2	0.2

[a]Not used in the final average.

However, the Dunhuang and Sechura sites yield significantly different values. This may in part be caused by an insufficient number of samples used to produce the trends, but may also be caused by real variations in the surface conditions at these sites.

Figure 7 shows the time series of normalized difference vegetation indices (NDVIs) for the Algerian

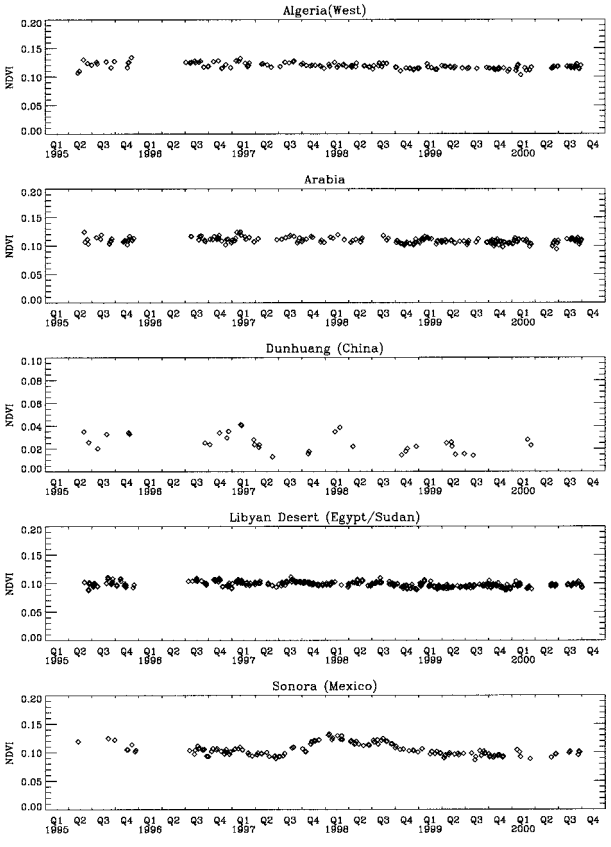

Fig. 7. Time series of NDVIs measured by ATSR-2 for the Algerian (West), Saudi Arabian, Dunhuang, southeastern Sudan, and Sonoran deserts.

(West), Arabian, Dunhuang, Libyan, and Sonoran desert sites where

$$\mathrm{NDVIs} = (R_{0.87\,\mu\mathrm{m}} - R_{0.66\,\mu\mathrm{m}})/(R_{0.87\,\mu\mathrm{m}} + R_{0.66\,\mu\mathrm{m}}). \quad (11)$$

The Algeria West, Arabian, and Libyan Desert sites are typical of all the North African sites with an average NDVI of ~0.1 with little variation. The Sonoran Desert also has an average NDVI of ~0.1, but shows a slight rise over the period between July 1997 to January 1999. As mentioned above, no data for the Sechura Desert were available after November 1997 because of severe flooding of the area resulting from the 1997 El Niño event. The surrounding area saw a significant increase in vegetation coverage normally associated with El Niño. Likewise, the rise in the NDVI observed for the Sonoran Desert coincides with the El Niño event, and it is well reported that the desert blossomed during this period. Although the drift values for this site were in agreement with the averages, the result was biased by the change in surface conditions. The NDVI for the Dunhuang Desert has a lower average NDVI of 0.03, but shows some significant variation about this value. Despite the relatively low number of samples, the variations of the NDVI appear to be seasonal with the peak values occurring around January of each year. Because of the variations observed in the NDVIs, the drift results from the Dunhuang, Sechura, and Sonoran deserts were not used for the final average.

Another feature of the results presented in Figs. 5 and 6 is the increase in scatter at shorter wavelengths that is due to the effect of dust and aerosols. Improving the reflectance model to include the effects of atmospheric scattering would reduce the scatter in the data, but would not necessarily affect the measured drift rate significantly. The data in Fig. 5 for the 0.56-μm channel show that the scatter is random and that the long-term trend is still clear.

6. Application of Drift Correction

For practical reasons, ATSR-2 visible channel images are calibrated with a look-up table consisting of a time series of a calibration factor F for the whole ATSR-2 mission. Conversion from digital number N to TOA reflectance R is simply

$$R = FN/\mu_0, \quad (12)$$

where

$$N = (C_{\mathrm{scene}} - C_{\mathrm{dark}})S/\mathrm{gain}, \quad (13)$$

$$F = R_{\mathrm{VISCAL}}\,\mathrm{gain}/[(C_{\mathrm{VISCAL}} - C_{\mathrm{dark}})S], \quad (14)$$

and S is a scaling factor used in the ATSR-2 data-processing system. The value of F used is that closest in time to the image acquisition. We apply the correction for long-term drift by modifying the calibration factor by

$$F' = F\exp(-kt/365) \quad (15)$$

using the average values of k given in Table 5.[15]

7. Conclusions

The long-term performance of the ATSR-2 VISCAL system has been measured with a number of radiometrically stable terrestrial targets. The drift rates observed were 0.3%, 1.1%, 1.1%, and 1.6%/yr for the 1.6-, 0.87-, 0.66-, and 0.56-μm channels, respectively. The drift correction has been incorporated into the ATSR-2 calibration scheme. Use of long time series and a range of sites reduces the impact of statistical fluctuations in the scene radiances and helps to identify the scene types most suitable for long-term monitoring and satellite intercomparisons. The results showed that the Sahara and Saudi Arabian desert sites were the most stable. The 1997 El Niño affected the Sonoran and Sechura deserts, and therefore their use for calibration was limited. The Greenland icecap was also a suitable site for the short-wavelength channels and gave drift rates that were in agreement with the desert sites.

The methods developed for this study will be applied for the ATSR that is due to be launched on ESA's Envisat mission in late 2001.

The authors thank Phil Watts of the Rutherford Appleton Laboratory (RAL) for advice on cloud clearing and Richard Siddans of RAL for extracting GOME ozone columns over Greenland. ATSR-2 data are provided courtesy of ESA, the Natural Environment Research Council, the British National Space Centre, and RAL. GOME data were provided courtesy of ESA and the German Aerospace Center.

References and Notes

1. G. McKay, M. D. Steven, and J. A. Clark, "An atmospheric correction procedure for the ATSR-2 visible and near-infrared land surface data," Int. J. Remote Sens. **19,** 2949–2968 (1998).
2. C. R. N. Rao and J. Chen, "Calibration of the visible and near-infrared channels of the Advanced Very High Resolution Radiometer (AVHRR) after launch," in *Recent Advances in Sensors, Radiometric Calibration, and Processing of Remotely Sensed Data*, P. S. Chavez and R. A. Schowengerdt, eds., Proc. SPIE **1938,** 56–66 (1993).
3. C. R. N. Rao and J. Chen, "Inter satellite calibration linkages for the visible and near infrared channels of the Advanced Very High Resolution Radiometer on the NOAA-7, -9 and -11 spacecraft," Int. J. Remote Sens. **16,** 1931–1942 (1995).
4. C. R. N. Rao and J. Chen, "Revised post-launch calibration of the visible and near-infrared channels of the Advanced Very High Resolution Radiometer on the NOAA-14 spacecraft," Int. J. Remote Sens. **20,** 3485–3491 (1999).
5. D. L. Smith, P. D. Read, and C. T. Mutlow, "The calibration of the visible/near infra-red channels of the Along-Track Scanning Radiometer-2 (ATSR-2)," in *Sensors, Systems and Next-Generation Satellites*, H. Fujisadsa, ed., Proc. SPIE **3221,** 53–62 (1997).

6. W. F. Staylor, "Degradation rates of the AVHRR visible channel for the NOAA 6, 7 and 9 spacecraft," J. Atmos. Oceanic Technol. **7,** 411–423 (1990).
7. B. N. Holben, Y. J. Kaufmann, and J. D. Kendall, "NOAA-11 AVHRR visible and near-IR inflight calibration," Int. J. Remote Sens. **11,** 1511–1519 (1990).
8. P. D. Read, A. L. Hardie, J. E. Magraw, H. S. Taylor, and J. V. Jelley, "A calibration system, using an opal diffuser, for the visual channels of the Along Track Scanning Radiometer, ATSR-2," Inst. Phys. Conf. Ser. **121,** 207–213 (1991).
9. N. G. Loeb, "In-flight calibration of NOAA AVHRR visible and near-IR bands over Greenland and Antarctica," Int. J. Remote Sens. **18,** 477–490 (1997).
10. H. Cosnefroy, M. Leroy, and X. Briottet, "Selection and characterisation of Saharan and Aarbian desert sites for the calibration of optical sensors," Remote Sens. Environ. **58,** 101–114 (1996).
11. D. Wu, Y. Yin, Z. Wang, X. Gu, M. Verbrugghe, and G. Guyot, "Radiometric characterisation of Dunhuang satellite calibration test site (China)," in *Physical Measurements and Signatures in Remote Sensing*, G. Guyot and T. Phulpin, eds. (Balkema, Rotterdam, The Netherlands, 1997), pp. 151–160.
12. S. M. Anderson and K. Mauersberger, "Laser measurement of ozone absorption cross sections in the Chappuis band," Geophys. Res. Lett. **19,** 933–936 (1992).
13. W. J. Wiscombe and S. G. Warren, "A model for the spectral albedo of snow. 1: Pure snow," J. Atmos. Sci. **37,** 2712–2745 (1980).
14. S. G. Warren, R. E. Brandt, and P. O. Hinton, "Effect of surface roughness on bidirectional reflectance of Antarctic snow," J. Geophys. Res. **103,** 25789–25807 (1998).
15. The modified version of the calibration tables, including these corrections, is available at the ATSR website http://www.atsr.rl.ac.uk.